

Geophysical Research Letters



RESEARCH LETTER

10.1029/2020GL090407

Key Points:

- We stress a gelatin block by excavating its surface and imposing lateral strain, then observe air-filled cracks trajectories
- We numerically simulate the trajectories and retrieve the stress state of the gelatin, then we forecast new crack arrivals at the surface
- Our strategy correctly retrieves the ratio between lateral extension and excavation depth and leads to effective forecasts of eruptive vents

Supporting Information:

- Supporting Information S1

Correspondence to:

L. Mantiloni,
lorenzo@gfz-potsdam.de

Citation:

Mantiloni, L., Davis, T., Gaete Rojas, A. B., & Rivalta, E. (2021). Stress inversion in a gelatin box: Testing eruptive vent location forecasts with analog models. *Geophysical Research Letters*, 48, e2020GL090407. <https://doi.org/10.1029/2020GL090407>





Received 17 AUG 2020

Accepted 3 FEB 2021

© 2021. The Authors.

This is an open access article under the terms of the [Creative Commons Attribution-NonCommercial License](https://creativecommons.org/licenses/by-nc/4.0/), which permits use, distribution and reproduction in any medium, provided the original work is properly cited and is not used for commercial purposes.

Stress Inversion in a Gelatin Box: Testing Eruptive Vent Location Forecasts With Analog Models

L. Mantiloni^{1,2} , T. Davis^{1,2} , A. B. Gaete Rojas¹ , and E. Rivalta¹ 

¹GFZ German Research Centre for Geosciences, Potsdam, Germany, ²University of Potsdam, Potsdam, Germany

Abstract Assessing volcanic hazard in regions of distributed volcanism is challenging because of the uncertain location of future vents. A statistical-mechanical strategy to forecast such locations was recently proposed: here, we further develop and test it with analog models. We stress a gelatin block laterally and with surface excavations, and observe air-filled crack trajectories. We use the observed surface arrivals to sample the distributions of parameters describing the stress state of the gelatin block, combining deterministic crack trajectory simulations with a Monte Carlo approach. While the individual stress parameters remain unconstrained, we effectively retrieve their ratio and successfully forecast the arrival points of subsequent cracks.

Plain Language Summary In regions of distributed volcanism, eruption locations (vents) are scattered over a large area. Forecasting the new eruption locations over such regions is critically important, as many are densely populated. One of the main difficulties is dealing with few known past eruptions, that is, the data available to constrain forecast models are scarce. Thus, we develop a forecast strategy by applying extension or compression to blocks of gelatin with surface excavations and observing the propagation of air-filled cracks. Such models, if properly scaled, are an analog for magma propagation in the Earth's crust. We use the surface arrival points of some observed cracks to retrieve the statistical distributions of a few parameters controlling the stress field. Next, we use such distributions to forecast the arrival points of other observed cracks. Although we could not retrieve all the stress parameters accurately, the forecasts we perform are reliable. Our strategy may help retrieving the state of stress in volcanic regions and forecast the location of future vents.

1. Introduction

In many volcanic regions, eruptive vents may be spatially scattered: they sometimes cluster along rift zones or are distributed over areas that may exceed 10,000 km². Some of these regions are densely populated. In order to better protect human life and infrastructure, it is important to better understand the factors determining vent distributions and improve vent location forecasts.

The most common approaches to probabilistic forecasts of future vent opening locations rely on the spatial density of past eruptive events, sometimes complemented with the surface distribution of structural features, such as faults and fractures (Bevilacqua et al., 2015; Connor & Hill, 1995; Martin et al., 2004; Selva et al., 2012). Such models, however, often remain poorly constrained due to scarce or spatially sparse data and cannot be easily validated in volcanic systems where eruptions are infrequent.

Recently, Rivalta et al. (2019) proposed a mechanical-statistical approach to inversely constrain the state of stress, and thus magma pathways, of a volcanic region on the basis of the known location of magma reservoirs and past eruptive vents. Dike trajectories are assumed to follow a “least resistance to opening” path calculated from the elastic stress field, which is optimized so that any magma batch released from the magma reservoir reaches one of the past eruptive vents. Once the stress field is constrained, the trajectories of future dikes can be forecast. Rivalta et al. (2019) applied the concept only to Campi Flegrei caldera in Italy, performing inversions on two stress parameters: namely, the tectonic and the unloading stress. As independent estimates of such parameters in nature are affected by large uncertainties, it remains unclear how accurately the model can capture them, how much other factors, such as medium layering, were biasing the results, and how this would affect the forecast.

Here, we delve deeper into the stress inversion concept, investigating these issues in a controlled setting: air-filled cracks propagating in a gelatin box. Such analog experimental setups have proven useful in validating dike propagation models (Maccaferri et al., 2019; Watanabe et al., 2002), for example, assessing the influence of surface loads (Gaete et al., 2019; J. R. Muller et al., 2001), rigidity layering (Maccaferri et al., 2010), and external stress fields (Acocella & Tibaldi, 2005). We stress the gelatin with extension/compression and surface excavations, shown in previous works to be the dominant stressing mechanisms in volcanic regions (Corbi et al., 2016; Maccaferri et al., 2014; Roman & Jaupart, 2014). Here, we do not intend to reproduce a specific geologic setting, but rather to test the ability of our strategy to retrieve the state of stress and the relative importance of surface excavations and regional stresses. We chose a valley-shaped surface geometry so that the stresses within the gelatin block can be approximated by plane strain, but our setup may provide insights on the same stress-generating mechanisms also in caldera-like settings. First, we run a series of experiments where we track the propagation of air-filled cracks. Second, we use a boundary element (BE) model to calculate expected crack trajectories with a realistic topography, combined with a Markov Chain Monte Carlo (MCMC) algorithm to sample two parameters describing the state of stress within the gelatin. This improves on Rivalta et al. (2019) both in terms of numerical modeling and sampling algorithm used. Third, we validate our strategy by running forecasts for additional cracks, which we compare to further injections.

2. Methods

2.1. Experimental Setup

We use a perspex container of size $A \times B \times C = 40 \times 20 \times 20$ cm (Figure 1a). We let a 2.0 wt% or 2.5 wt% aqueous solution of 220 Bloom pig gelatin powder solidify in the box at $T = 8$ °C for 20 h. These concentration values are well characterized in previous works (e.g., Di Giuseppe et al., 2009; Gaete et al., 2019; Kavanagh et al., 2013; Smittarello, 2019). Along the y -direction, the gelatin block surface is molded to include a rectangular excavation of width $w = 6$ –7 cm and varying depth h (Figure 1a), causing surface unloading (Gaete et al., 2019). The height of the gelatin block, H , varied throughout the experiments (see Figure 1a). Compression or extension were imposed on the set gelatin by inserting or removing two plastic plates of thickness $d = 2.5 \pm 0.1$ mm at the box sides, separated from the medium by a transparent plastic film (Figure 1a). We chose $d = \pm 2.5$ mm both to work with a small strain, $e = 2 d/A$, and to obtain ratios between stresses due to extension/compression and unloading comparable with estimates in nature (see Section 2.2).

Air is injected into the gelatin from the bottom of the box, resulting in ascending air-filled cracks. Different injections are made through different holes at 1 cm intervals, both to avoid the reopening of previous cracks and to observe trajectories over as wide a section of the gelatin block as possible. Air has often been used as a magma analog in gelatin-based models (Corbi et al., 2016; Menand et al., 2010). Air is nearly inviscid, so that trajectories are not influenced by viscous effects, which are investigated in other works (e.g., Pintel et al., 2019; Smittarello, 2019). All experiments were carried out at room temperature, with timescales short enough (≤ 1 h) to maintain the experiments in an elastic regime (Kavanagh et al., 2013). The Young's modulus E of the gelatin was determined case by case by applying a small cylindrical load on the surface and measuring the resultant subsidence under the assumption of a half space (Kavanagh et al., 2013). E was mostly within the 2,000–3,500 Pa range (supporting information, Table S2). We assumed the Poisson's ratio is $\nu = 0.49$ (van Otterloo & Cruden, 2016) and take $\rho_{\text{gel}} = 1,020$ kg m⁻³ for the gelatin density (Smittarello, 2019). We attached polarized sheets on the box front and back walls (Figure 1c) to observe stress inhomogeneities during the experiments. The resulting sequences of colored fringes (Table 1) visualize the differential stress ($\sigma_1 - \sigma_3$) perpendicular to the light direction (Gaete et al., 2019).

We present seven experiments (2DLA- i , $i = 1, \dots, 7$), involving extension (2DLA-1,3,4,5,6,7), compression (2DLA-2) and layering (2DLA-3,4). Three more experiments with compression were discarded as most of the cracks hit the box walls (see Figure S4). We measure the surface arrival points of the cracks (x_i^{obs}). In 2DLA-5,6,7, we changed the state of stress midway in the experiments: we performed N^f injections, then removed the side plates (2DLA-5) or partially refilled the surface excavation with water (2DLA-6,7), and finally injected N^f more cracks (see Table 1 and Figure S2). The data from 2DLA-6 and 2DLA-7 were also

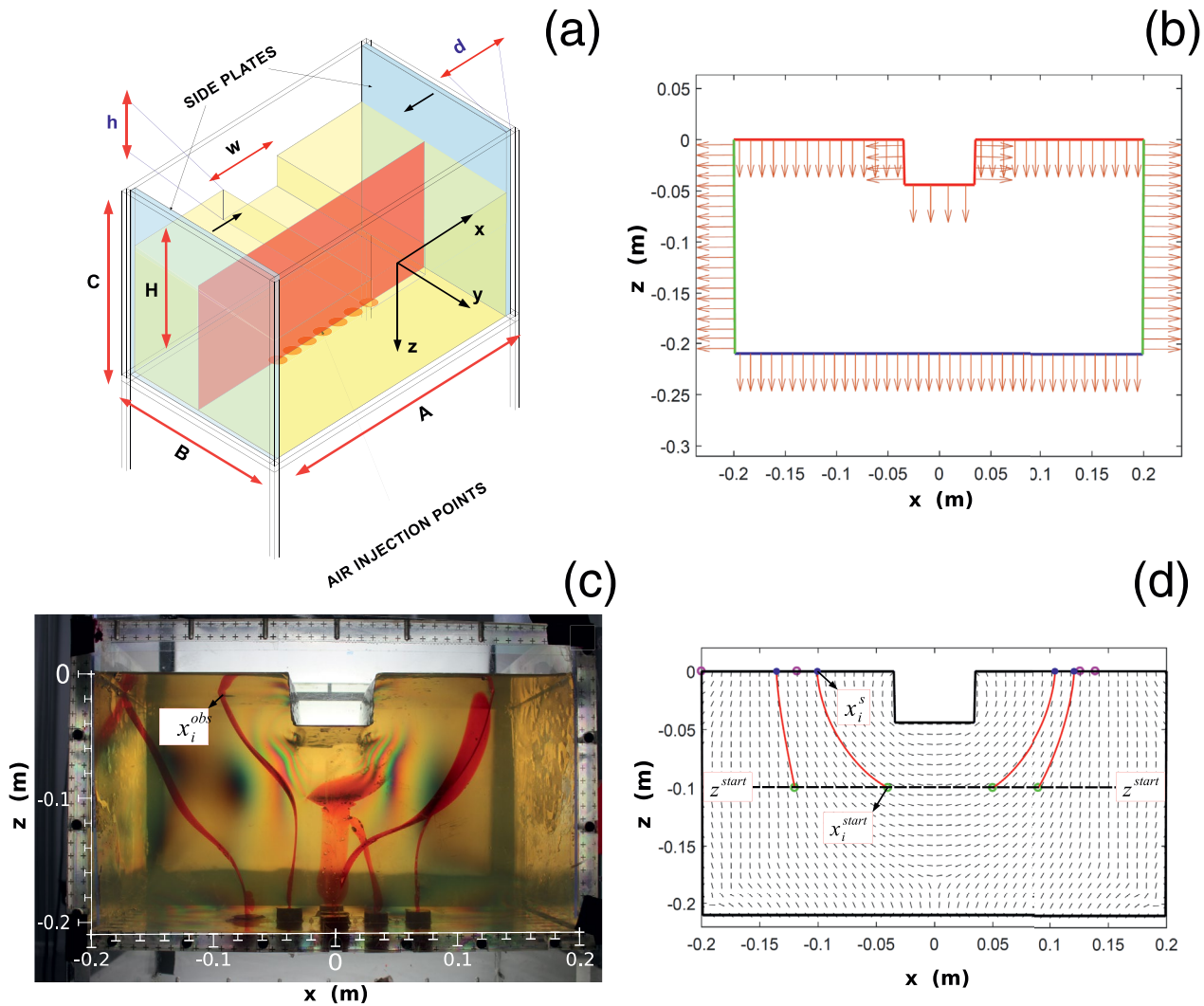


Figure 1. (a) Schematic view of the gelatin box: the side plates are highlighted in blue, the median plane of the block in red. The quantities are defined in Section 2.3. (b) Discretization of the box and its surface over the median plane. Arrows: normals to BEs. The length of the illustrated BEs is larger than the one we employed. (c) Front view of the gelatin box at the conclusion of experiment 2DLA-2 (compression): crack trajectories are marked post-intrusion with red ink. (d) Numerical simulation of 2DLA-2 (c) from random parameters: x_i^s are marked with blue dots, x_i^{obs} with magenta circles. Simulated trajectories are highlighted in red and σ_1 directions are drawn in black. z^{start} is marked by a black dashed line. BE, boundary element.

pooled to test the method with a larger data set. All the respective data sets are collected in the supporting information and published as a separate data publication (Mantiloni et al., 2021).

Inhomogeneities of various nature affect the outcome of the experiments. Some of them are unplanned, such as temperature differences up to $\sim 3^\circ\text{C}$ between the gelatin surface and the bottom (see Table S2), leading to differences in the Young's modulus (≤ 600 Pa) that are of the same order of, or may exceed, the uncertainties on our measures (van Otterloo & Cruden, 2016), and localized strain concentrations induced when removing and, especially, inserting the side plates. Conversely, rigidity layering is intentionally introduced in experiments 2DLA-3 & 2DLA-4 (Table 1): elastic interfaces were welded by pouring a $\sim 25^\circ\text{C}$ second layer (Kavanagh et al., 2017). In 2DLA-3, the bottom layer had a higher gelatin concentration, and thus rigidity, than the top one, and reverse in 2DLA-4. The Young's modulus E of the bottom and top layers was measured and estimated from other measurements for the same concentration, respec-

tively (Table S2). For these two experiments, we assume a homogeneous medium in the numerical model and an “effective” Young’s modulus obtained by carrying out the measurement on the whole block. The aim here was to test the performance of the strategy when ignoring an existing layered structure in the simulations.

2.2. Scaling

The length scaling factor between our experiments and nature is given by the buoyancy length (Secor & Pollard, 1975):

$$L = \left(\frac{K_c}{\frac{1}{\pi^2} \Delta \rho g} \right)^{\frac{2}{3}} \quad (1)$$

where K_c is the medium fracture toughness and $\Delta \rho$ is the density contrast between the host medium and the injected fluid. Taking $\Delta \rho_r = 100 \text{ kg m}^{-3}$, $\Delta \rho_{gel} = 1,000 \text{ kg m}^{-3}$ as the rock-magma and gelatin-air density contrasts, respectively, $K_c^r = 0.2 - 1 \cdot 10^9 \text{ Pa} \cdot \text{m}^{\frac{1}{2}}$ as the rock fracture toughness and $K_c^{gel} = 60 - 80 \text{ Pa} \cdot \text{m}^{\frac{1}{2}}$ for a gelatin with Young’s modulus in the range of $E = 2,000 - 3,000 \text{ Pa}$ (Kavanagh et al., 2013; Smittarello, 2019), we obtain $L^* = 3.3 \times 10^{-6} - 1.2 \times 10^{-5}$, where the asterisk refers to the ratio between analog and natural values. Thus, the excavation width range $w = 6 - 7 \text{ cm}$ we measured (Table S2) corresponds to 6–20 km in nature, compatible with the broad range of lateral scales (100 m–100 km) displayed by unloading mechanisms on Earth, such as the development of rifts or calderas or icecap melting. Likewise, a typical starting depth of 100–150 mm (Table 1) corresponds to 10–50 km in nature. Such a starting depth for dikes is deep but not unreasonable. The stress scaling factor is calculated by dividing the unload stress $\sigma_U = \rho_{gel}gh$ for the excavation in the gelatin by the one for the natural case. Taking $h = 2 - 5 \text{ cm}$ (Table 1) and excavations 0.1–1 km deep, assuming $\rho_r = 2,500 \text{ kg m}^{-3}$, we obtain $\sigma^* = 8 \times 10^{-6} - 1 \times 10^{-4}$. We also require the ratio between the stresses arising from lateral strain and the unloading to be comparable to natural cases. In our experiments, such ratio $Ee/\rho_{gel}gh$, where $e = 2d/A = 1.25 \times 10^{-2}$, is in the range 0.04–0.31. The same ratio in nature, for rifts or calderas 100–1,000 m deep, assuming $\rho_r = 2,500 \text{ kg m}^{-3}$ and a typical range for absolute values of tectonic stresses of 1–10 MPa (Heidbach et al., 2016), is 0.04–4.00, which comprises our experimental range, even if the latter lies close to its lower limit. An overview of our scaling factors is reported in the supporting information (Table S1).

2.3. Numerical Modeling

We assume an elastic rheology in the numerical model. This is commonplace in previous works (Anderson, 1937; O. H. Muller & Pollard, 1977; Roman & Jaupart, 2014) and supported by field observations on dikes (Gudmundsson, 2002; Lister & Kerr, 1991). There is, however, evidence of nonelastic dike propagation in nature (Poppe et al., 2020; Spacapan et al., 2017), which is reproduced in different analog models (e.g., Poppe et al., 2019).

To calculate the elastic stresses within the gelatin, we use the two-dimensional (2D) BE code “Cut&Displace” (Crouch et al., 1983; Davis et al., 2017, 2019). We approximate the experiment’s geometry as plane strain, as we observed no strain in the analog model’s y-direction (Figure 1a). The box bottom, top and walls are discretized into BEs of length $l_{BE} = 2 \text{ mm}$ (Figure 1b). Displacement is set to zero on the bottom elements, while we impose fixed displacement on the side walls, equal to d or $-d$ for extension or compression, respectively. The free surface is shaped to model the excavation; stress boundary conditions are imposed on them to reproduce the gravitational stress due to the unload (Martel & Muller, 2000, Equation 1). We assume that w and the position of the excavation are known exactly, and we employ the measured values of E for each experiment. In the data pooling of 2DLA-6&7 (see Section 2.1), we assumed for E and h the arithmetic mean of the respective values from the two experiments, as these were similar but not identical (Table 1).

We calculate the principal stress directions on a dense grid of observation points within the box. We simulate the crack trajectories assuming that the cracks open against, and propagate perpendicular to, the least compressive stress axis, σ_3 (Anderson, 1951). This assumption makes a good approximation of real trajectories provided the size and volume of the cracks are not too large (Maccaferri et al., 2019; Watanabe et al., 2002) and the effects of viscosity can be neglected, as well as those of external stress gradients (Dahm, 2000). The more these assumptions are far from reality, the larger the mismatch between real and σ_3 -perpendicular trajectories. More complex dike trajectory models exist for simulations in 2D (Dahm, 2000; Maccaferri et al., 2011) and recently also in three dimensions (3D) (Davis et al., 2020). However, the predictive power of models increases if their complexity is reduced with regard to accurate explanatory dike trajectory models (see e.g., Forster & Sober, 1994). Thus, we opt for the simpler option of σ_3 -perpendicular trajectories, which also necessitate much shorter computation time and better serve the stochastic part of our strategy.

If the cracks are misaligned with the stress field at injection, they will require some distance to realign (Maccaferri et al., 2019; Menand et al., 2010). The starting depth in the simulations is shallower than the injection depth so that this readjustment occurs at least partly.

2.4. MCMC Scheme

Our sampling procedure relies on the Delayed Rejection and Adaptive Metropolis MCMC algorithm (Haario et al., 2006; Laine, 2013). The set of N observed arrivals (x_i^{obs} , $i = 1, \dots, N$) is first divided into two subsets N^I and N^F (“I” and “F” stand respectively for “inversion” and “forecast”). The N^I set is used to sample the two parameters d and h . The size of our data sets varies from a minimum $N^I = 2$ in 2DLA-2 to a maximum of $N^I = 5$ in 2DLA-6&7 (see the supporting information, Tables S3–S4).

At start, ranges and guesses for the parameters d and h are fixed together with a common starting depth for the cracks, z^{start} . Starting locations, x_i^{start} , are assigned as the horizontal coordinate of the upper tips of the observed cracks at z^{start} . At each iteration, we simulate N^I crack trajectories and sample d and h in order to minimize the objective function

$$S = \sum_{i=1}^{N^I} \left(x_i^s - x_i^{obs} \right)^2 \quad (2)$$

where x_i^s are the simulated arrivals.

The squares of the uncertainties on the two parameters ($\Delta d = \pm 0.1$ mm; $\Delta h = \pm 1$ mm) populate the diagonal of the covariance matrix. $M = 10^4$ iterations were made for every chain. Our runs highlight a correlation between d and h , as expected from Rivalta et al. (2019), so we consider a further parameter: $R = d/h$, which partly removes the trade-off, and use the posterior probability distributions (PPDs) of d and R to perform the forecasts.

2.5. Forecasting Approach

After performing the inversions, we run $M^F = 10^3$ iterations of N^F simulations for the forecasts, where we sample the parameters (d , R) from their PPDs. Starting points are drawn from Gaussian distributions centered on $x_i^{start,F}$, $z_i^{start,F}$, with standard deviation $\sigma = 1$ mm. The combined distribution of simulated arrivals is compared to the observed arrivals set aside for the forecast $x_i^{obs,F}$. We measure the success of a forecast from how far the median $x_i^{med,F}$ of the simulated arrivals lies from $x_i^{obs,F}$. Thus, for each individual i -th forecast, we define $\Delta x_i^F = \left| x_i^{obs,F} - x_i^{med,F} \right|$ and compare it to the standard deviation δx_i^F of the distribution (see Table 1).

A different approach is adopted in experiments 2DLA-5 and 2DLA-6&7 to account for the modified state of stress between the N^I and N^F cracks. In 2DLA-5, we fit the PPDs of d and R with Beta functions and then update them by shifting the mean value and their upper and lower limits to account for the added extension (from $d = 0$ mm to $d = 2.5$ mm). In 2DLA-6&7, we use the same strategy, except that we update h (subtracting the height of the water filling the surface excavation) and R .

3. Results

3.1. Experimental Results and Numerical Modeling

Experiments with extension and compression resulted in markedly different observations. Surface unloading deflects vertical crack trajectories, as seen in both natural (Corbi et al., 2015; Tibaldi, 2004) and experimental (Corbi et al., 2016; Gaete et al., 2019) settings. Regional extension competes against the former, leading to more vertical trajectories (Maccaferri et al., 2014). Compression, instead, tends to rotate σ_1 to horizontal (Menand et al., 2010), thus amplifying the effect of the unloading. The effect of extension is observed in 2DLA-5, where extension was applied after N^f cracks had propagated, by comparing green (early) to red (late) trajectories (Table 1). The partial refilling in experiments 2DLA-6 and 2DLA-7 (Table 1) reduced the influence of the unloading and led to less deflected trajectories. Trajectory simulations for the experiments with extension are not identical to, but closely match the observations, if the measured d and h are employed.

Trajectories in compressional settings (2DLA-2 and discarded experiments, see Figure S3) tend to diverge significantly from each other and spread the uncertainty of the initial location into scattered arrival locations. Simulations with the imposed parameters fail to reproduce these data sets. This is reflected in the outcome of the inversions and forecasts, as we explain later on.

Dike trajectories are deflected toward the vertical direction when passing from a high-rigidity layer to a low-rigidity one and viceversa, as theoretically predicted by Maccaferri et al. (2010) (see experiments 2DLA-3 and 2DLA-4, Table 1).

3.2. Parameters Sampling

We find that in most cases the retrieved PPDs fail to constrain d and h individually, though they generally succeed in constraining their ratio R . This can be seen in the joint distributions for R and h (Figure 2a). In the homogeneous extensional cases, the PPDs for d and especially h are generally spread. In spite of this, the imposed value of d is well recovered in 2DLA-5 and 2DLA-6 & 7 (see Table S5). The distributions of h tend to be uniform. In contrast, the PPD for R is always peaked around or close to the imposed value (Figure 2a). The PPDs, including those of h , are more peaked when more data are available (2DLA-6&7). In the layered cases, the medians of all the PPDs are rather far from the respective imposed values, except for R in 2DLA-4. This was expected, since we purposely neglected the medium layering in the modeling (see Section 2.1).

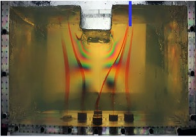
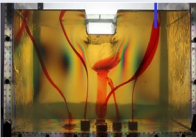
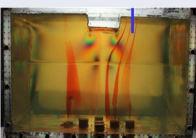
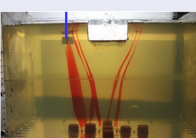
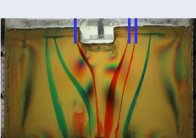
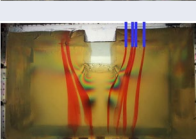
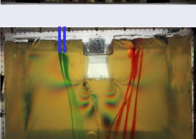
In the only compressional case (2DLA-2), the PPDs are extremely spread and fail to constrain the parameters, though the median of R is close to the imposed value (Figure 2a).

3.3. Forecasts

In spite of the PPDs for d and h being often spread or even uniform, the forecast distribution generally shows N^f sharp peaks (Figure 2b and Table 1). Moreover, in spite of the PPDs for d and h failing to accurately recover the imposed values, the peaks of the forecast distribution generally coincide or are very close to the observed arrivals (Figure 2b and Table 1). This includes the layered cases. Again, the compressional case 2DLA-2 marks an exception: the forecast is rather spread (see δx_i^F values in Table 1) and shows two maxima, one closer to the box center and a sharp one at the box margin (Figure 2b); this is due to the fact that many simulated cracks hit the right side of the box. Neither of the maxima coincides with the observed arrival, and the median falls ~ 1 cm away (Figure 2b and Table 1).

Two secondary peaks are also obtained in the combined forecast distribution for 2DLA-5 ($N^f = 3$), as the sampling range for d allowed for both positive (extension) and negative (compression) values. This is reflected also in the spread of the individual distributions (Table 1). The two main maxima are here close to the box center and show good agreement with $x_i^{obs,F}$. Considering the three individual distributions separately, the distances $\Delta x_i^{obs,F}$ between the three $x_i^{obs,F}$ and the medians $x_i^{med,F}$ are well within $\delta x_i^{obs,F}$ of the respective distributions. In 2DLA-6&7 ($N^f = 6$), three clear maxima are observed in the combined forecast

Table 1
Experiments, Measured Parameters, and Results

Experiments		Measured parameters			Results			Forecasts		
# Exp.	Picture	h	d	R	h^{med}	d^{med}	R^{med}	$x_i^{med,F}$	δx_i^F	Δx_i^F
		± 1	± 0.1	$(\times 10^{-3})$			$(\times 10^{-3})$			
		mm	mm		mm	mm		mm	mm	mm
2DLA-1 Extension		50	2.5	63 ± 4	51	4.9	100	67	7	2
2DLA-2 Compression		44	-2.5	-57 ± 4	73	-3.5	-55	115	39	11
2DLA-3 Extension Layered		21	2.5	120 ± 10	63	3.9	69	75	9	1
2DLA-4 Extension Layered		24	2.5	104 ± 8	59	5.8	102	-85	6	1
2DLA-5 Updated Extension		24	0 2.5	0 ± 10^{-2} 104 ± 8	64	0.4	8×10^{-3}	-54 66 77	43 36 34	1 6 10
2DLA-6 Extension Refilled		58(65) 28(35)	2.5(2.5)	(39 ± 2) (71 ± 7)	64	2.5	39	63 76 84 102	10 7 6 4	3 1 2 1
2DLA-7 Extension Refilled		72(65) 32(35)	2.5(2.5)	(39 ± 2) (71 ± 7)				-84 -73	8 6	4 0

Note. Blue markers in the pictures indicate the arrivals used for the forecast (see Figure 2b): in 2DLA-5, 2DLA-6, and 2DLA-7 these coincide with the injections following the stress update (differently colored trajectories in pictures of 2DLA-5 and 2DLA-7 stand for preupdate and postupdate). Arithmetic means assumed for h and R in 2DLA-6&7 are indicated in parentheses (Section 2.3). Updated d and h (Section 2.5) are in boldface. h^{med} , d^{med} , R^{med} : medians of the respective PPDs (Section 3.2). $x_i^{med,F}$, δx_i^F , and Δx_i^F are defined in Section 2.5 and refer to forecasts for individual $x_i^{obs,F}$. For further information, see the supporting information, Tables S2–S4 (measured quantities) and S5 (inversion results).
Abbreviation: PPD, posterior probability distribution.

distribution, showing again good agreement with the $x_i^{obs,F}$, which are ≤ 4 mm away from the medians of the respective individual distributions (Table 1).

In all extensional experiments with $N^F = 1$, the observed arrivals $x_i^{obs,F}$ are always within 2 mm from the medians (Table 1).

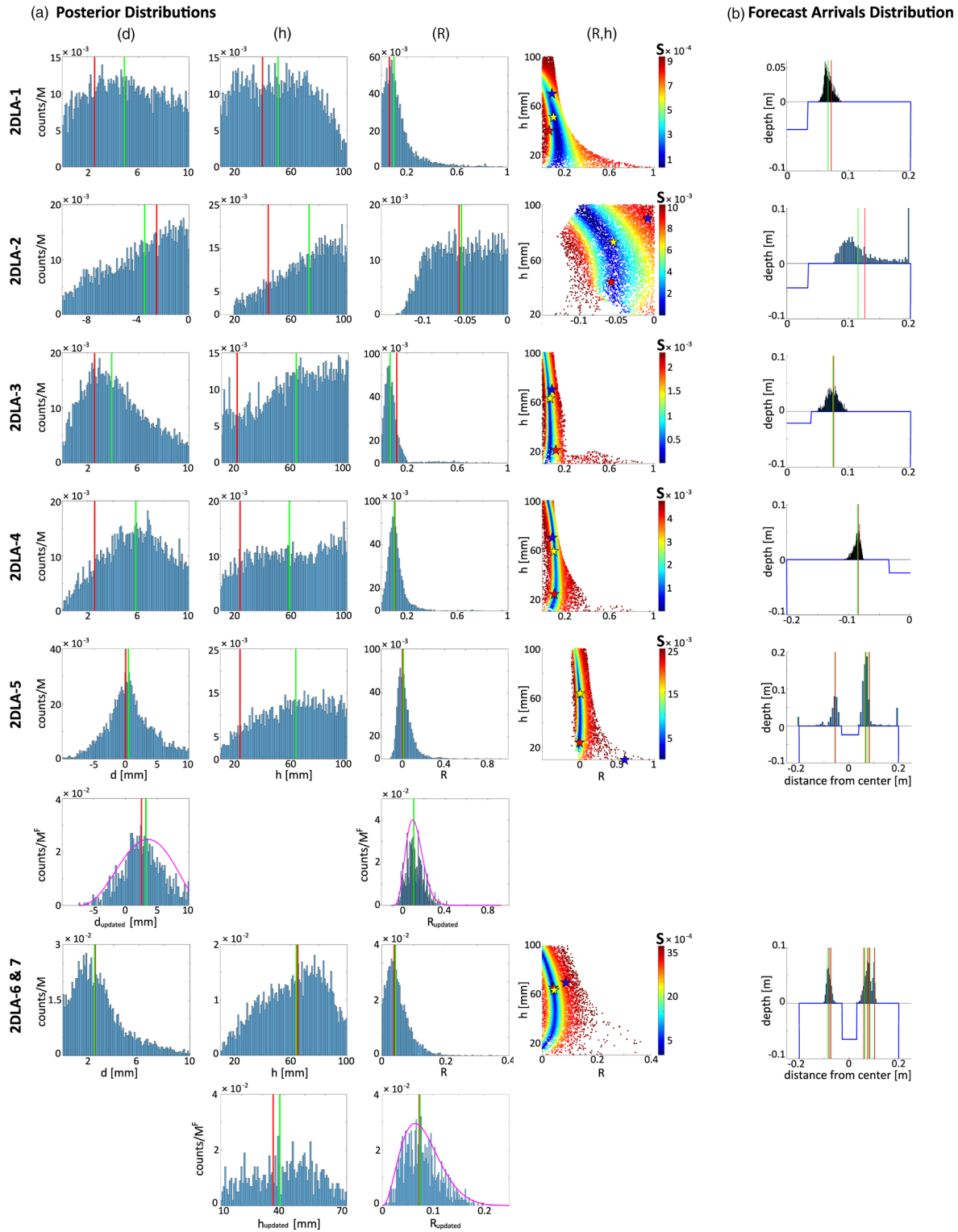


Figure 2. Summary of inversion and forecast results. (a) PPDs for parameters d , h and R and joint PPD for (R, h) . Red lines show the measured values; green lines the medians (Table 1). The Beta functions used to fit and update the distributions in 2DLA-5 and 2DLA-6&7 are plotted in magenta. Last column from left: the starting guess, measured and median values are represented, respectively, by a blue, red and yellow star. The color palette shows the value of S (Equation 2) for every sampled point in the parameters' space, from dark red (higher S) to blue (lower S). (b) countings of forecast arrivals displayed on a scheme of the box (the surface topography shown is before the refilling in 2DLA-6&7). Red lines: positions of $x_i^{obs,F}$; green lines: medians of the forecasts for individual $x_i^{obs,F}$ (see also Tables 1 and S3). PPD, posterior probability distribution.

4. Discussion

While the inversion algorithm generally failed to retrieve the imposed values of the parameters d and h (Figure 2a), the forecast strategy proved very effective in identifying high-probability regions for crack arrivals on the surface (Table 1 and Figure 2). This apparent contradiction arises from the fact that the inversions effectively recover the imposed value of $R = d/h$. Physically, this is because the curvature of the trajectories is controlled by R , rather than d or h individually, as also found by Roman and Jaupart (2014).

Forecasts are successful in spite of scarce data sets and when layering of the medium is neglected. If data sets are larger (5 data points for 2 parameters), the state of stress is recovered more accurately. In principle, our procedure could be used also to constrain the elastic parameters, but information on the stress state would be necessary as they trade off. To test this possibility, we ran an inversion for E on the N^F data set of 2DLA-5, and we found the sampled E distribution peaks very close to the measured value (results are shown in Figure S4b).

The forecast strategy applied in experiments 2DLA-5 and 2DLA-6&7 also proved effective in accounting for the modification of the stress field over time, validating the evolving-stress forecast method by Rivalta et al. (2019).

Several factors may contribute to the failure of the approach in compressional settings, even though there is inherently no difference in the σ_3 -perpendicular propagation of cracks under remote compression rather than extension. Both unloading and compression lead to more horizontal σ_1 directions within the medium. Thus, the mismatch between the crack orientation and σ_1 right after the injection is larger and they need more space to align. Moreover, a horizontal σ_1 may encourage cracks to propagate toward the back or the front walls of the box, whose effect on the gelatin may undermine the plane strain assumption (in compressional cases, these walls prevent the gelatin to expand along the y -axis, thus inducing compression also in this direction). Furthermore, side plate insertion and the nonfrictionless contact between gelatin and box walls induced local stress concentrations at the box corners, affecting nearby trajectories (Figure S3). Such effects may arise from the size of our box and could be reduced by employing a larger tank. However, as σ_3 -perpendicular trajectories tend to diverge in compressional settings (including nature), simulations are more sensitive to any variability of initial and boundary conditions or model parameters, and forecasts are therefore more challenging.

A further limitation arises from the limited number of experiments we carried out. In spite of this, we did observe clear common patterns in experiments with similar settings (Section 3.1). Our experimental setup allowed for several factors, including variable starting crack length and orientation, elastic heterogeneities and possible interactions between successive injections, to play a role. This is reflected in the fact that observed and modeled trajectories do not coincide in general (Section 3.1), though the forecasts are fairly good. This is not contradictory, as our forecast strategy includes a stochastic model to treat such variability.

Another remarkable issue is the nearly uniform trend observed in the PPDs for h (Figure 2a), which appears to be systematic even when larger data sets are available (as opposed to the PPDs of d , cfr 2DLA-1, and 2DLA-5). This arises from the fact that very shallow or very deep surface unloads, for the same d and starting points, lead to similar arrivals. We surmise that this effect, observed both in the numerical simulations and in a separate experiment (Figure S4a), is due to the relaxation of the surface excavation's walls under gravity.

5. Conclusive Remarks

We conclude that a mixed deterministic-stochastic strategy is effective in constraining the ratio of different stress-generating mechanisms and forecasting the arrival points of air-filled cracks in gelatin blocks. The strategy performs well on small data sets and may be, therefore, suitable for applications to volcanic regions where few vent locations are available. Future developments may focus on relaxing some of the limitations in our current numerical simulations, such as upgrading to 3D, including the viscous flow in the cracks, or addressing rheologies different from elastic. This will facilitate direct application to producing probabilistic maps of vent location for volcanic systems in nature.

Data Availability Statement

All data employed in this work are available at the GFZ Data Services repository: GFZ.2.1.2021.001 <https://doi.org/10.5880/GFZ.2.1.2021.001> (Mantiloni et al., 2021). The numerical model is based on the open source code at <https://doi.org/10.5281/zenodo.3694164>.

Acknowledgments

The authors are grateful to Thierry Menand and Sam Poppe, whose thorough and constructive reviews greatly improved the quality of our work. L. Mantiloni and T. Davis are funded by the grants N. RI 2782/6-1—ZO 277/3-1 and DFG-ICDP N. RI 2782/3-1, respectively.

References

- Acocella, V., & Tibaldi, A. (2005). Dike propagation driven by volcano collapse: A general model tested at Stromboli, Italy. *Geophysical Research Letters*, 32(8). <https://doi.org/10.1029/2004GL022248>
- Anderson, E. M. (1937). IX.—the dynamics of the formation of cone-sheets, ring-dykes, and caldron-subsidences. *Proceedings of the Royal Society of Edinburgh*, 56, 128–157. <https://doi.org/10.1017/S0370164600014954>
- Anderson, E. M. (1951). *The dynamics of faulting and dyke formation with applications to Britain*. Hafner Pub. Co.
- Bevilacqua, A., Isaia, R., Neri, A., Vitale, S., Aspinall, W. P., Bisson, M., et al. (2015). Quantifying volcanic hazard at Campi Flegrei caldera (Italy) with uncertainty assessment: 1. Vent opening maps. *Journal of Geophysical Research: Solid Earth*, 120(4), 2309–2329. <https://doi.org/10.1002/2014JB011775>
- Connor, C. B., & Hill, B. E. (1995). Three nonhomogeneous Poisson models for the probability of basaltic volcanism: Application to the Yucca Mountain region, Nevada. *Journal of Geophysical Research*, 100, 10107–10125. <https://doi.org/10.1029/95JB01055>
- Corbi, F., Rivalta, E., Pinel, V., Maccaferri, F., & Acocella, V. (2016). Understanding the link between circumferential dikes and eruptive fissures around calderas based on numerical and analog models. *Geophysical Research Letters*, 43(12), 6212–6219.
- Corbi, F., Rivalta, E., Pinel, V., Maccaferri, F., Bagnardi, M., & Acocella, V. (2015). How caldera collapse shapes the shallow emplacement and transfer of magma in active volcanoes. *Earth and Planetary Science Letters*, 431, 287–293. <https://doi.org/10.1016/j.epsl.2015.09.028>
- Crouch, S. L., Starfield, A. M., & Rizzo, F. (1983). *Boundary element methods in solid mechanics*.
- Dahm, T. (2000). Numerical simulations of the propagation path and the arrest of fluid-filled fractures in the earth. *Geophysical Journal International*, 141, 623–638. <https://doi.org/10.1046/j.1365-246x.2000.00102.x>
- Davis, T., Healy, D., Bubeck, A., & Walker, R. (2017). Stress concentrations around voids in three dimensions: The roots of failure. *Journal of Structural Geology*, 102, 193–207. <https://doi.org/10.1016/j.jsg.2017.07.013>
- Davis, T., Healy, D., & Rivalta, E. (2019). Slip on wavy frictional faults: Is the 3rd dimension a sticking point? *Journal of Structural Geology*, 119, 33–49. <https://doi.org/10.1016/j.jsg.2018.11.009>
- Davis, T., Rivalta, E., & Dahm, T. (2020). Critical fluid injection volumes for uncontrolled fracture ascent. *Geophysical Research Letters*, 47(14). <https://doi.org/10.1029/2020GL087774>
- Di Giuseppe, E., Funicello, F., Corbi, F., Ranalli, G., & Mojoli, G. (2009). Gelatins as rock analogs: A systematic study of their rheological and physical properties. *Tectonophysics*, 473(3–4), 391–403. <https://doi.org/10.1016/j.tecto.2009.03.012>
- Forster, M., & Sober, E. (1994). How to tell when simpler, more unified, or less ad hoc theories will provide more accurate predictions. *The British Journal for the Philosophy of Science*, 45, 1–35. <https://doi.org/10.1093/bjps/45.1.1>
- Gaete, A., Kavanagh, J. L., Rivalta, E., Hazim, S. H., Walter, T. R., & Dennis, D. J. (2019). The impact of unloading stresses on post-caldera magma intrusions. *Earth and Planetary Science Letters*, 508, 109–121. <https://doi.org/10.1016/j.epsl.2018.12.016>
- Gudmundsson, A. (2002). Emplacement and arrest of sheets and dykes in central volcanoes. *Journal of Volcanology and Geothermal Research*, 116(3–4), 279–298. [https://doi.org/10.1016/S0377-0273\(02\)00226-3](https://doi.org/10.1016/S0377-0273(02)00226-3)
- Haario, H., Laine, M., Mira, A., & Saksman, E. (2006). Dram: Efficient adaptive MCMC. *Statistics and Computing*, 16(4), 339–354. <https://doi.org/10.1007/s11222-006-9438-0>
- Heidbach, O., Rajabi, M., Reiter, K., Ziegler, M., & Team, W. (2016). *World stress map database release 2016*. GFZ Data Services. <https://doi.org/10.5880/WSM.2016.002>
- Kavanagh, J., Menand, T., & Daniels, K. A. (2013). Gelatine as a crustal analogue: Determining elastic properties for modeling magmatic intrusions. *Tectonophysics*, 582, 101–111. <https://doi.org/10.1016/j.tecto.2012.09.032>
- Kavanagh, J., Rogers, B., Boutelier, D., & Cruden, A. (2017). Controls on sill and dyke-sill hybrid geometry and propagation in the crust: The role of fracture toughness. *Tectonophysics*, 698, 109–120. <https://doi.org/10.1016/j.tecto.2016.12.027>
- Laine, M. (2013). *Mcmc toolbox for matlab, 2013*. URL: <http://helios.fmi.fi/~lainema/mcmc>.
- Lister, J. R., & Kerr, R. C. (1991). Fluid-mechanical models of crack propagation and their application to magma transport in dykes. *Journal of Geophysical Research*, 96, 10049–10077. <https://doi.org/10.1029/91JB00600>
- Maccaferri, F., Bonafede, M., & Rivalta, E. (2010). A numerical model of dyke propagation in layered elastic media. *Geophysical Journal International*, 180(3), 1107–1123. <https://doi.org/10.1111/j.1365-246X.2009.04495.x>
- Maccaferri, F., Bonafede, M., & Rivalta, E. (2011). A quantitative study of the mechanisms governing dike propagation, dike arrest and sill formation. *Journal of Volcanology and Geothermal Research*, 208(1–2), 39–50. <https://doi.org/10.1016/j.jvolgeores.2011.09.001>
- Maccaferri, F., Rivalta, E., Keir, D., & Acocella, V. (2014). Off-rift volcanism in rift zones determined by crustal unloading. *Nature Geoscience*, 7(4), 297–300. <https://doi.org/10.1038/ngeo2110>
- Maccaferri, F., Smittarello, D., Pinel, V., & Cayol, V. (2019). On the propagation path of magma-filled dikes and hydrofractures: The competition between external stress, internal pressure, and crack length. *Geochemistry, Geophysics, Geosystems*, 20(4), 2064–2081. <https://doi.org/10.1029/2018GC007915>
- Mantiloni, L., Davis, T., Gaete, A., & Rivalta, E. (2021). *Gelatin-based analog models simulating dike propagation in the upper crust*. GFZ. <https://doi.org/10.5880/GFZ.2.1.2021.001>
- Martel, S. J., & Muller, J. R. (2000). A two-dimensional boundary element method for calculating elastic gravitational stresses in slopes. *Pure and Applied Geophysics*, 157(6–8), 989–1007. <https://doi.org/10.1007/s000240050014>
- Martin, A. J., Umeda, K., Connor, C. B., Weller, J. N., Zhao, D., & Takahashi, M. (2004). Modeling long-term volcanic hazards through Bayesian inference: An example from the Tohoku volcanic arc, Japan. *Journal of Geophysical Research*, 109(B10). <https://doi.org/10.1029/2004JB003201>
- Menand, T., Daniels, K., & Benghiat, P. (2010). Dyke propagation and sill formation in a compressive tectonic environment. *Journal of Geophysical Research*, 115(B8). <https://doi.org/10.1029/2009JB006791>
- Muller, J. R., Ito, G., & Martel, S. J. (2001). Effects of volcano loading on dike propagation in an elastic half-space. *Journal of Geophysical Research*, 106, 11101–11113. <https://doi.org/10.1029/2000JB900461>

- Muller, O. H., & Pollard, D. D. (1977). The stress state near spanish peaks, colorado determined from a dike pattern. *Pure and Applied Geophysics*, 115, 69–86. <https://doi.org/10.1007/BF01637098>
- Pinel, V., Smittarello, D., Maccaferri, F., Rivalta, E., & Cayol, V. (2019). Stress field control on magma path and velocity. *American Geophysical Union, Fall Meeting 2019*.
- Poppe, S., Galland, O., de Winter, N., Goderis, S., Claeys, P., Debaille, V., et al. (2020). Structural and geochemical interactions between magma and sedimentary host rock: The hovedøya case, oslo rift, norway. *Geochemistry, Geophysics, Geosystems*, 21(3). e2019GC008685. <https://doi.org/10.1029/2019GC008685>
- Poppe, S., Holohan, E. P., Galland, O., Buls, N., Van Gompel, G., Keelson, B., et al. (2019). An inside perspective on magma intrusion: Quantifying 3d displacement and strain in laboratory experiments by dynamic x-ray computed tomography. *Frontiers in Earth Science*, 7, 62. <https://doi.org/10.3389/feart.2019.00062>
- Rivalta, E., Corbi, F., Passarelli, L., Acocella, V., Davis, T., & Di Vito, M. A. (2019). Stress inversions to forecast magma pathways and eruptive vent location. *Science advances*, 5(7). eaau9784. <https://doi.org/10.1126/sciadv.aau9784>
- Roman, A., & Jaupart, C. (2014). The impact of a volcanic edifice on intrusive and eruptive activity. *Earth and Planetary Science Letters*, 408, 1–8. <https://doi.org/10.1016/j.epsl.2014.09.016>
- Secor, D. T., Jr, & Pollard, D. D. (1975). On the stability of open hydraulic fractures in the earth's crust. *Geophysical Research Letters*, 2, 510–513. <https://doi.org/10.1029/GL002i011p00510>
- Selva, J., Orsi, G., Di Vito, M. A., Marzocchi, W., & Sandri, L. (2012). Probability hazard map for future vent opening at the campi flegrei caldera, italy. *Bulletin of Volcanology*, 74(2), 497–510. <https://doi.org/10.1007/s00445-011-0528-2>
- Smittarello, D. (2019). *Propagation des intrusions basaltiques. modélisation analogique et suivi temporel par inversion des données de déplacements (Unpublished doctoral dissertation)*. Université Grenoble Alpes.
- Spacapan, J. B., Galland, O., Leanza, H. A., & Planke, S. (2017). Igneous sill and finger emplacement mechanism in shale-dominated formations: A field study at cuesta del chihuido, neuquén basin, argentina. *Journal of the Geological Society*, 174(3), 422–433.
- Tibaldi, A. (2004). Major changes in volcano behavior after a sector collapse: Insights from stromboli, italy. *Terra Nova*, 16(1), 2–8. <https://doi.org/10.1046/j.1365-3121.2003.00517.x>
- van Otterloo, J., & Cruden, A. R. (2016). Rheology of pig skin gelatine: Defining the elastic domain and its thermal and mechanical properties for geological analogue experiment applications. *Tectonophysics*, 683, 86–97. <https://doi.org/10.1016/j.tecto.2016.06.019>
- Watanabe, T., Masuyama, T., Nagaoka, K., & Tahara, T. (2002). Analog experiments on magma-filled cracks. *Earth Planets and Space*, 54(12), 1247–1261. <https://doi.org/10.1186/BF03352453>